

EXPERIMENTAL RESULTS OF GROUND DISTURBANCE DETECTION USING UNCOOLED INFRARED IMAGERS IN WIDEBAND AND MULTISPECTRAL MODES

Philips Laou

Defence R&D Canada, 2459 Pie-XI Blvd North, Québec, Qc G3J 1X5 Canada
philips.laou@drdc-rddc.gc.ca

KEYWORDS: surveillance, detection, multispectral, LWIR, ground disturbance

ABSTRACT:

We investigated the feasibility of using uncooled infrared (IR) imagers in multispectral and wideband imaging for ground disturbance detection. Samples of sand, soil and mixture of both were used in the experiments. The multispectral imaging was carried out using IR bandpass filters. A software tool was used to process wideband and multispectral images to determine sample temperature contrast from which we examined effects due to reststrahlen features or other phenomena. A two-point, side-by-side scanning scheme showed possible ground disturbance detection by picking up substantial contrast when the two-point was entering and exiting the disturbed zone.

1. INTRODUCTION

In an ongoing effort of design and development of multispectral uncooled IR detectors, we investigated in this work the use of multispectral imaging for ground disturbance detection. We performed experiments to study ground disturbance detection using multispectral imaging. Multispectral imaging was carried out using several IR bandpass filters and a wideband uncooled LWIR imager. These results will allow us to access the potential of the use of an uncooled LWIR imager to detect reststrahlen features or other phenomena associated with ground disturbance.

1.1 Previous Work on Buried Object and Soil Disturbance Detection

There were detailed studies in mid-90s on buried object detection using passive IR technologies. Commercial cooled midwave IR (MWIR) and longwave IR (LWIR) cameras were used in wide

band (WB) in all these studies. For example, LWIR images showed, even a week after the burial, buried anti-tank and anti-personnel mines under specific environmental conditions [1]. Several theoretical modelings were investigated and experimentally validated on buried mines signature using MWIR and LWIR cameras [2-4]. As the performance of low cost, uncooled IR imagers becomes better, there have been trials recently in 2007 using uncooled LWIR imager for surface and buried land mine detection [5].

There are other activities on buried object detection using hyperspectral imaging technologies [6], for example, on LWIR hyperspectral surface-laid mine detection [7,8]; and on hyperspectral imaging of various bands (very near IR or VNIR and shortwave IR or SWIR) for mine detection [9].

1.2 Reststrahlen Effect

Detection of soil disturbance for clues on the possible mine presence was considered one of the feasible approaches without the effort of detecting the buried objects. 16 spectral features were defined from VNIR, SWIR, MWIR to LWIR for soil disturbance detection [10]. Among the 16, four of them were considered having the greatest potential. The quartz reststrahlen band in the 8 to 10 μ m is among the four.

Reststrahlen refers to the selectively reflection of light from the surface of a transparent solid when the frequency of the light is nearly equal to the vibration frequency of the ions in the crystalline solid. In the case of quartz or sand, the reststrahlen feature is weaker at around 8-9.5 μ m in a disturbed region leading to higher emissivity (higher absorption or lower reflection). It was shown that disturbed soil exhibits a considerable change in IR emissivity between 8-9.5 μ m, and this could persist for several weeks [11]. There have been studies using an airborne IR hyperspectral instrument to characterize

Report Documentation Page			Form Approved OMB No. 0704-0188		
Public reporting burden for the collection of information is estimated to average 1 hour per response, including the time for reviewing instructions, searching existing data sources, gathering and maintaining the data needed, and completing and reviewing the collection of information. Send comments regarding this burden estimate or any other aspect of this collection of information, including suggestions for reducing this burden, to Washington Headquarters Services, Directorate for Information Operations and Reports, 1215 Jefferson Davis Highway, Suite 1204, Arlington VA 22202-4302. Respondents should be aware that notwithstanding any other provision of law, no person shall be subject to a penalty for failing to comply with a collection of information if it does not display a currently valid OMB control number.					
1. REPORT DATE 01 FEB 2012		2. REPORT TYPE		3. DATES COVERED 00-00-2012 to 00-00-2012	
4. TITLE AND SUBTITLE Experimental Results of Ground Disturbance Detection Using Uncooled Infrared Imagers in Wideband and Multispectral Modes			5a. CONTRACT NUMBER		
			5b. GRANT NUMBER		
			5c. PROGRAM ELEMENT NUMBER		
6. AUTHOR(S)			5d. PROJECT NUMBER		
			5e. TASK NUMBER		
			5f. WORK UNIT NUMBER		
7. PERFORMING ORGANIZATION NAME(S) AND ADDRESS(ES) Defence R&D Canada - Valcartier, 2459 Pie-XI Blvd North, Quebec (Quebec) G3J 1X5 Canada,			8. PERFORMING ORGANIZATION REPORT NUMBER ; DRDC-VALCARTIER-SL-2012-		
9. SPONSORING/MONITORING AGENCY NAME(S) AND ADDRESS(ES)			10. SPONSOR/MONITOR'S ACRONYM(S)		
			11. SPONSOR/MONITOR'S REPORT NUMBER(S) DRDC-VALCARTIER-SL-2012-		
12. DISTRIBUTION/AVAILABILITY STATEMENT Approved for public release; distribution unlimited					
13. SUPPLEMENTARY NOTES					
14. ABSTRACT We investigated the feasibility of using uncooled infrared (IR) imagers in multispectral and wideband imaging for ground disturbance detection. Samples of sand, soil and mixture of both were used in the experiments. The multispectral imaging was carried out using IR bandpass filters. A software tool was used to process wideband and multispectral images to determine sample temperature contrast from which we examined effects due to reststrahlen features or other phenomena. A two-point, sideby-side scanning scheme showed possible ground disturbance detection by picking up substantial contrast when the two-point was entering and exiting the disturbed zone.					
15. SUBJECT TERMS					
16. SECURITY CLASSIFICATION OF:			17. LIMITATION OF ABSTRACT Same as Report (SAR)	18. NUMBER OF PAGES 12	19a. NAME OF RESPONSIBLE PERSON
a. REPORT unclassified	b. ABSTRACT unclassified	c. THIS PAGE unclassified			

reststrahlen effect of buried mines. Fig. 1 replicated a calculated spectral emissivity from hyperspectral imaging measurement for a disturbed and undisturbed soil sample with mine buried on a road [12]. The soil sample was analyzed and showed sand/quartz content, and showed similar results in the MODIS (Moderate Resolution Imaging Spectrometer) UCSB Emissivity Library at various locations [13]. With the use of the Planck equation and the emissivity shown in Fig. 1, we can estimate the temperature difference caused by reststrahlen band.

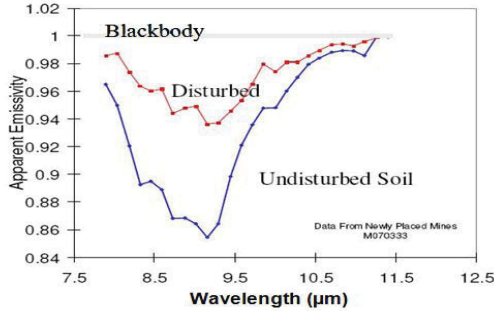


Figure 1. Spectral emissivity of undisturbed and disturbed soil with buried mine [12].

The Plank equation for blackbody spectral exitance $M_\lambda(\lambda, T)$ (unit in $\text{W}/\text{cm}^2\text{-}\mu\text{m}$) is shown in Eq. 1.

$$M_\lambda(\lambda, T) = \varepsilon \frac{2\pi hc^2}{\lambda^5 \left[e^{\frac{hc}{\lambda kT}} - 1 \right]} \quad (1)$$

ε , emissivity, is equal to 1 for a blackbody; h , Planck's constant, is equal to 6.6×10^{-34} J-s; c , speed of light, is equal to 3×10^8 m/s; k , Boltzmann's constant, is equal to 1.38×10^{-23} J/K. The total exitance M can be determined by integrating Eq. 1 over 7.5 to 13.5 μm . It is equal to $\sim 1.79 \times 10^{-2}$ Watt/cm^2 . Referring to Fig. 1, emissivity of disturbed and undisturbed soil are 0.94 and 0.86 at 9 μm , respectively. With the knowledge of the blackbody spectral exitance at 9 μm at 300K, the emissivity, and the use of Eq. 1, we can compute the apparent temperatures of the disturbed and undisturbed soil temperatures. The blackbody (300K) spectral exitance M_λ at 9 μm is 3.13×10^{-3} $\text{Watt}/\text{cm}^2\text{-}\mu\text{m}$. The corresponding spectral exitance of the disturbed and undisturbed soil are equal to 2.94×10^{-3} and 2.69×10^{-3} $\text{Watt}/\text{cm}^2\text{-}\mu\text{m}$. At these exitance levels, the

apparent undisturbed soil temperature observed with the same WB camera behind a 9 μm bandpass filter will be $\sim 213\text{K}$ and the disturbed one $\sim 217\text{K}$ in temperatures. A 300K black body observed at 9 μm with the same WB camera will have an apparent temperature of $\sim 218\text{K}$. This result showed that the presence of reststrahlen band should cause at least several degrees difference in temperature between disturbed and undisturbed soil. An uncooled IR imager with sufficient sensitivity (Noise equivalent of temperature difference or NETD) at around 100mK NETD should be sufficiently sensitive to measure this temperature difference.

2. EQUIPMENT AND EXPERIMENT SETUP

2.1. IR Imager, Filters and Imager Temperature Sensitivity in Bandpass Mode

Uncooled LWIR imager:

The LWIR uncooled imager is the Photon OEM core from Indigo Inc. It is a 324 by 256 VOx uncooled microbolometer camera with a pixel size of 38 μm . The spectral range is from 7.5 to 13.5 μm . A 19mm lens was purchased with the camera providing a 36 (H) by 27 (V) degrees field-of-view and at F/1.4 optics. NETD of the imager is $<85\text{mK}$ at F/1.6 and 30 frames per second. It is noted that the relation between NETD and F/# is:

$$\text{NETD} \propto (F/\#)^2 \quad (2)$$

Therefore, the NETD of the current imager at F/1.4 is ~ 65 mK. The lens diameter is 19.5mm and the front aperture is 13mm. An Ethernet module from Indigo was used to control the Photon imager and this allows us to capture the images digitally at 14-bit resolution via a user interface by a computer. An adaptor was made and mounted to the front of the imager aperture for LWIR filter insertion (Fig. 2).



Figure 2. Picture showing the Photon imager, filter adaptor and an IR filter.

Table 1. LWIR filters.

Filter description	Centre λ (nm)	¹ Bandwidth (nm)	Ave Transmission (%)	Peak Transmission (%)
² BP-8645-550nm (A)	8636.9	554.9	86.82	86.87
BP-8835-335nm (B)	8814.4	329.2	83.48	83.54
BP-9130-500nm (C)	9111.3	464.2	81.24	81.3
BP-9260-500nm (D)	9271.1	474.7	81.97	82.02
³ NB-9645-220nm (E)	⁴ 9610	⁴ 260		⁴ 83.1
BP-9965-675nm (F)	9935.8	724.6	69.14	77.64
NB-10350-460nm (G)	⁴ 10320	⁴ 495		⁴ 87.1
BP-10600-250nm (H)	⁴ 10615	⁴ 285		⁴ 71.7

1. Bandwidth at FWHM=Full-width-half-maxi; 2. BP=Band pass; 3. NB=Narrow band; 4. Result measured at DRDC laboratory using a spectrometer due to missing original data from supplier.

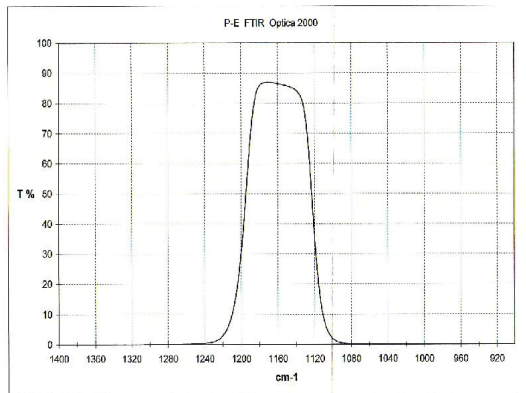


Figure 3. This is the transmission chart of BP8645-550nm (A).

LWIR filters:

LWIR filters (25.4mm in diameter) were purchased from Spectrogon Inc (Tab. 1). They can be mounted and interchanged in front of the imager aperture using the filter adaptor. These filters are assigned the symbols from A to H, respectively. As an example, the transmission chart of BP-8645-550nm or filter A is shown in Fig. 3. The profile of other filters are very similar.

Imager temperature sensitivity in bandpass mode:

NETD is defined as the temperature difference (ΔT) for which the signal-to-noise ratio (SNR)

equals to 1 where the signal is proportional to radiance L (watt/cm²-ster) while noise level is known. The NETD of the imager, however, will degrade when it operates at narrow band as less L will enter the imager and receive by the detector leading to weaker detected signal. By considering Stefan-Boltzmann law, an imager NETD and its $\partial L / \partial T$ (the change in radiance per unit temperature) associated over 7.5 to 13.5 μ m (response range of the IR imager), and the use of bandpass filters, we can determine the modified NETD due to the use of bandpass filters. The modified NETD were presented in Tab. 2. The NETD degradation is from the original 65mK in WB operation to a range between 538 and 1972mK in bandpass mode. We can see that E and H may not provide sufficient sensitivity for contrast measurement.

Table 2. Modified NETD of the imager and the associated bandpass filters.

Filter description	$\partial L / \partial T$ for the specified bandwidth (Watt/cm ² -ster-K)	Corresponding NETD (mK)
BP-8645-550nm (A)	9.2×10^{-6}	643
BP-8835-335nm (B)	5.4×10^{-6}	1095
BP-9130-500nm (C)	8.9×10^{-6}	665
BP-9260-500nm (D)	8.8×10^{-6}	672
NB-9645-220nm (E)	3.4×10^{-6}	1740
BP-9965-675nm (F)	1.1×10^{-6}	538
NB-10350-460nm (G)	7.8×10^{-6}	758
BP-10600-250nm (H)	3.0×10^{-6}	1972

2.2. Pyranometer

Heat exchange rate and apparent temperature contrast are governed by factors such as solar radiation and air temperatures, we must measure the solar radiation during the trial. For example, strong solar radiation and warmer air in mid-day will lead to the optimum day (OD) condition resulting in a high apparent temperature contrast which favors detection. The solar radiation was measured by a CMP11 pyranometer manufactured by Kipp & Zonen. The radiation reflection from the surface was not measured in this trial to determine the net radiation absorption by the soil. Local air temperature and humidity were measured and noted during the trial.

2.3. Soil, Sand and Boxes

Three plywood boxes were prepared with a dimension of 48 (W) by 48 (L) by 15 (H) inches. The three boxes contain 100% soil (~10% stones) excavated at DRDC Valcartier site, 100% sand (general purpose sand from Marco, product of Canada) and a mixture of 50/50 of soil and sand.

2.4. Experimental Setup and Procedure

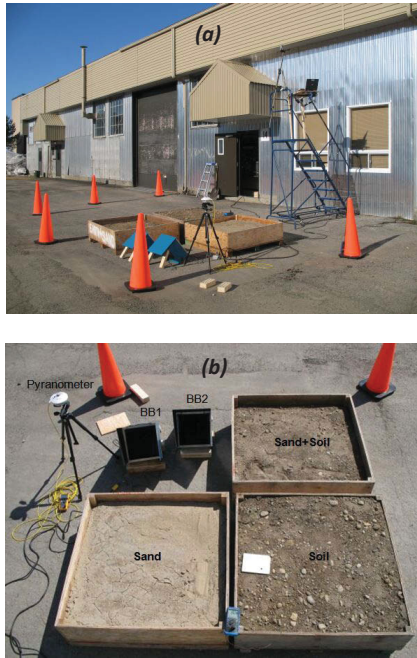


Figure 4. (a) The experimental setup and (b) positions of experimental items.

Fig. 4 (a) shows the views of the experimental setup. The IR imager was mounted on a stage about 150 inches from the ground where it pointed downward viewing the sand boxes and the two black bodies. The pyranometer was positioned close to the sand boxes. Fig. 4 (b) indicates the position of all the items in the imaging area. The square metal plate in the soil box is to facilitate focus adjustment of the IR imager.

We have performed measurements over a three-day period (April 15-17, 2008). On April 15, we monitored the environment condition since morning. The soil was disturbed at 13h30 and followed by two IR image capturing sessions. The soil was again disturbed at 11h10 and 10h10 on April 16 and 17 before noon, respectively. This is to allow a few more image capturing sessions between the soil disturbance in the morning and

the end of the day. In addition, we may be able to observe the degradation of disturbed soil IR signature, and the relationship between the solar radiation and time of disturbed soil.

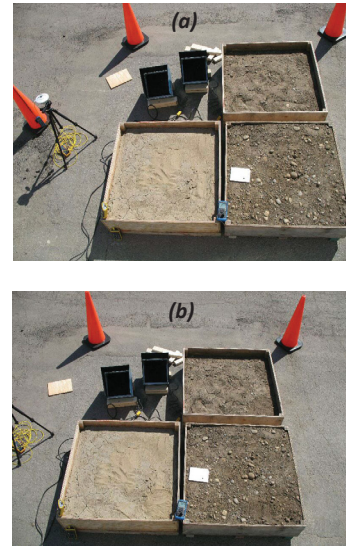


Figure 5. Pictures of the three samples (a) before and (b) after disturbance (Right bottom corner).

Each day, the soil was first disturbed either at the centre or corner of the sand boxes. We took precaution disturbing the soil so that it is as indistinguishable as possible examined by naked eyes. Fig. 5 (a) and (b) are pictures showing pre- and post-disturbance (bottom right corners in all three) in visible band. They were taken at 11h00 (pre-disturbance) and 11h20 (post-disturbance) on April 16 2008. We then immediately started the IR image capturing session. First, ambient temperature, humidity, solar radiation, and soil temperatures both near the surface (~1cm deep) and deeper (~15cm deep) from the surface were measured using thermocouples and multimeters. One black body was set to the ambient temperature while the other was set at several degrees above ambient temperature. Then, we started to capture IR images with and without IR filters. We then waited for about an hour to repeat the steps.

3. SOIL TEMPERATURE ESTIMATION

Two temperature-referenced black bodies scheme was used to determine the temperature of soil in the boxes. A software tool based on this principal was used to process the images. This tool is called *Windows Infrared Signature Analysis Software (WinISAS v3.0)*. It was developed by Louis Tanguay Informatique (LTI) in 2004.

3.1. Determining Pixel Temperatures

We first assume that the pixel intensity is proportional to the scene temperature it images. Then, one black body was set to this temperature ($T_{Ambient}$) while a second one was set at several degrees above the ambient temperature ($T_{Ambient+}$). With the knowledge of the black body temperatures and the intensity in digital values ($I_{Pixel@BB_ambient}$ and $I_{Pixel@BB_ambient+}$) of the corresponding pixels imaging the black bodies, we can determine the slope m of a calibration line. We also need to know the temperature T_{Int} , when intensity is zero, or the intercept of the calibration curve at the temperature, in order to determine the scene temperature seeing by the pixel.

$$T_{Int} = T_{BB_ambient+} - m * I_{Pixel@BB_ambient+} \quad (6)$$

With this information, the temperature seeing by the pixel, T_{Pixel_Y} , can be computed. I_{Pixel_Y} is the intensity at $Pixel_Y$. The principal of computing the pixel temperature can be best illustrated in Fig. 6.

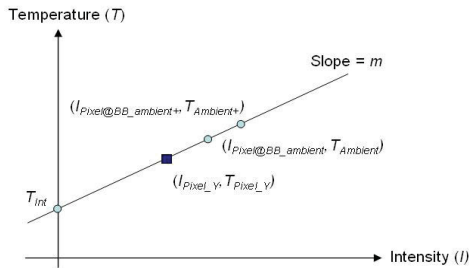


Figure 6. The principal of computing the temperature seeing by the pixel.

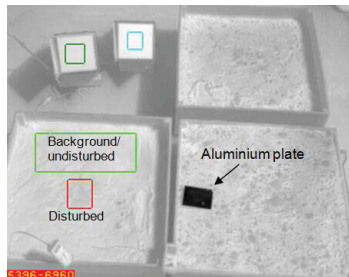


Figure 7. A typical IR image showing designated regions under analysis by WinISAS.

We have to make sure that the imager is not saturated by very high temperature scenery, or the temperature calculation based on two-point linearity is false. The video signal (NTSC) was measured at the maximum scene temperature of 43 °C and the analog signal was at ~0.66V which

is still below the saturation level of 0.7V. As a result, the imager was never saturated.

Fig. 7 (taken on April 15 2008) illustrates a typical IR image analyzed by WinISAS in which we indicated the regions of the two black bodies (top left corner) and then entered the corresponding temperatures. The undisturbed (green) and disturbed (red) regions were also indicated in the IR image where the sand box was located. An average of pixel temperatures within the marked green and red rectangle regions (user selected) was calculated based on the pixel intensity and black bodies temperatures, providing the black body equivalent temperatures (B.E.T.) or the corresponding undisturbed and disturbed region temperatures and temperature contrast.

4. RESULTS AND DISCUSSIONS

4.1. Solar Radiation

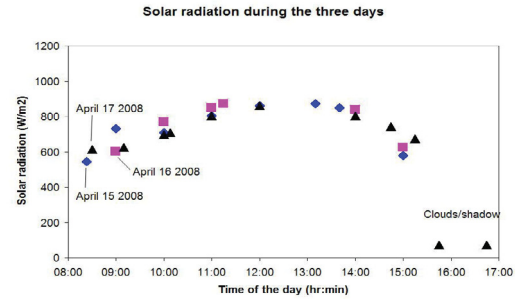


Figure 8: Solar radiation during the three-day measurement.

As the soil temperature depends on the solar radiation, we need to monitor the latter so that we can relate it to the measured contrast. Fig. 8 shows the solar radiation of the experiments during the three days. We can see that the three curves are quite similar. We will refer to this recorded solar radiation if necessary in the data analysis.

4.2. Experimental Data Analysis– Contrast

Using the contrast data, we made plots to show the relationship between contrast, lapsed time, filters used, and types of sample. Before the analysis, however, we would like to make a few comments on the general phenomenology of heat exchange of this test. It is noted that all boxes were left outdoor the night before the trials. In April time, the ambient temperature is around 0 °C during the nights in Québec (Eastern Canada). As a result, the bulk sand and soil samples in the boxes were cold. In the early morning, the surface

of the samples warmed up slightly by the sun and increased ambient temperature but the temperature increase is slower below the surface. We measured using thermocouples the sand temperatures about 8cm below the surface and near the surface. On April 16, they were 1.6 and 13 °C, 1.4 and 19 °C, 2.9 and 29 °C, 6.2 and 37 °C, 7.8 and 38 °C, and 10.8 and 32 °C, at 9h00, 10h00, 11h00, 13h00, 14h00, and 15h00, respectively. Over the three days, the surface temperature rose by ~20 to 30 °C while ~5 to 10 °C below the surface between mornings and late afternoons. The surface heats up a lot faster. In addition, when we dig the soil to induce a disturbance, the cold sand/soil beneath was overturned and exposed. As a result, the disturbed regions were colder than the surrounding and this led to negative contrast at the beginning, and in some cases throughout the trial. We also know that the water (high specific heat capacity material) content in the samples plays a role in the heating rate of the samples, and this has influence on the contrast values. In our test, the sand sample containing little water heated up faster than the soil and sand/soil samples during the day. On April 16, for example, the WB B.E.T. of sand raised from 18 to 32 to 37 °C while soil from 17 to 28 to 34 °C at 9h00, 11h20 and 13h00, respectively. As we have no knowledge of the spectral emissivity of the samples, detailed interpretation of the phenomenology related to absolute temperature and heating rate is not studied here. Interpretation is mainly focused on contrast data of the three samples.

Contrast Variation of the samples – April 16 to 17 2008:

Fig. 9 (a) to (c) show the temperature contrast characteristics of the sand, soil, and the mixture samples with the use of different IR bandpass filters as a function of time, followed by disturbance at 11h10 on April 16.

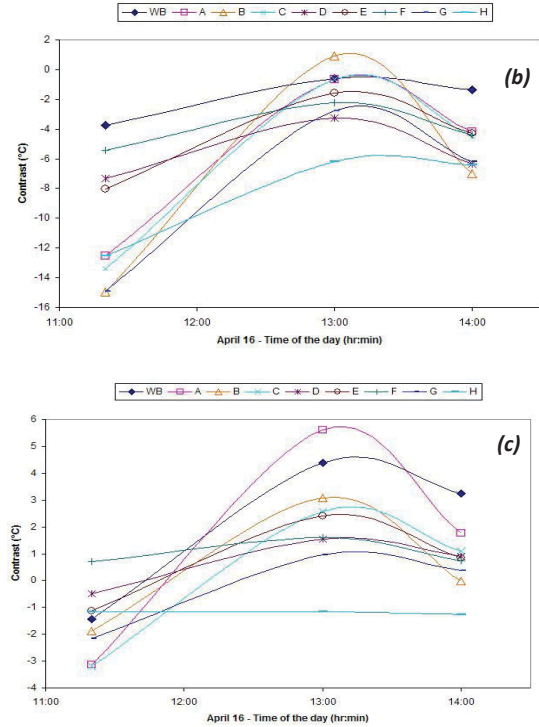
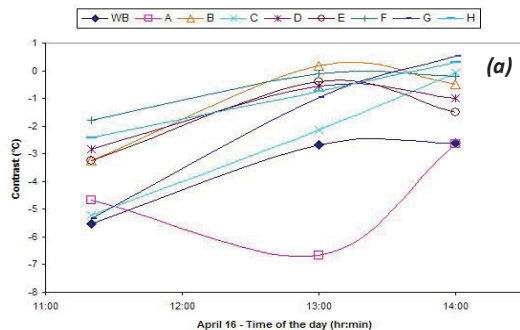


Figure 9. Calculated contrast between disturbed and undisturbed regions of (a) sand; (b) soil; and (c) sand/soil samples with different IR filters.

The trends of the curves are very similar except the one obtained from the sand sample using Filter A. This point is not considered further in the analysis. In general, all contrast began with the most negative values of the day. It is because all overturned sand, and/soil and soil regions were relatively colder. The disturbed soil sample appeared to be the coldest in WB and throughout all filters measurement at 11h20 (For example, measuring in WB, soil at 23.9 °C compared to sand at 26.7 °C measured at 11h20; while using Filter A, soil at 12.5 °C compared to sand at 23.1 °C measured at 11h20), leading to most negative contrast. This is possibly due to the high water content in the soil.

In all samples, contrast became less negative, or decreased, toward midday as the cold, disturbed regions heated up together with the undisturbed regions. In the case of sand, the apparent temperature of the disturbed region barely reach that of the undisturbed region (or background) at 13h00 only to level beyond this point when the solar radiation began to drop from 13h00 to 14h00. From the sand sample, we could see large contrast in WB and as well with Filters A and C. In the sand/soil sample, contrast became positive, or the disturbed region temperatures were higher

than the background. This could be attributed possibly to the fact that the water presence in the soil and the increased emissivity of the disturbed region (reststrahlen band) resulted in high target temperatures and larger contrast.

This effect is most significant at 13h00 with the use of Filter A where the measured contrast with Filter A is positive and larger than that in WB measurement. We can also see that the target temperatures of the sand/soil samples are higher in WB, and with Filters A and C, at 13h00 (38.6, 32.2, 34.6 °C) and 14h00 (36.2, 31.0, 35.6 °C) compared to the sand (34.5, 26.2, 21.5 °C at 13h00 and 33.0, 27.7, 31.5 °C at 14h00) and soil samples (33.8, 26.2, 22.5 °C at 13h00 and 31.3, 20.1, 25.7 °C at 14h00). On the other hand, the temperatures of disturbed soil sample were always lower than the soil background (WB, Filters A-H), and were lower (WB, Filters A and C) than those of sand/soil and sand targets at 11h20, 13h00 and 14h00. The reason could be that the initial temperatures of soil target were low to begin with, and the water content (high heat capacitance) makes the overturned soil sample to heat up slower and less. It is interesting to see that, with the use of filters, the contrast is more significant in both positive and negative compared to WB measurement from 11h20 to 14h00.

After the last measurement at 14h00 on April 16, the three sample boxes were left outdoor for the night. In the following day on April 17, a few more measurements were made on the same disturbed regions in order to see the lasting effect, if any, on contrast due to reststrahlen features or other phenomena associated with disturbed soil. On April 17, the solar radiation was about the same as that of April 16 (Fig. 10), however, the ambient temperature was higher. This made the test samples to heat up faster and reach higher temperatures. For example, the ambient temperature (sun exposure) was 16.4 °C and that of sand surface was 27 °C on April 17 at 10h08, compared to 9.7 °C and 19 °C, respectively, on April 16 at 10h00. The sand sample reached above 40 °C on the surface between 13h00 and 14h00 and beyond while the maximum temperature on April 16 was below 38 °C. Fig. 10 (a) to (c) show the contrast characteristics of the three samples. Filter E was broken during the test and no data can be collected using it in part of this measurement.

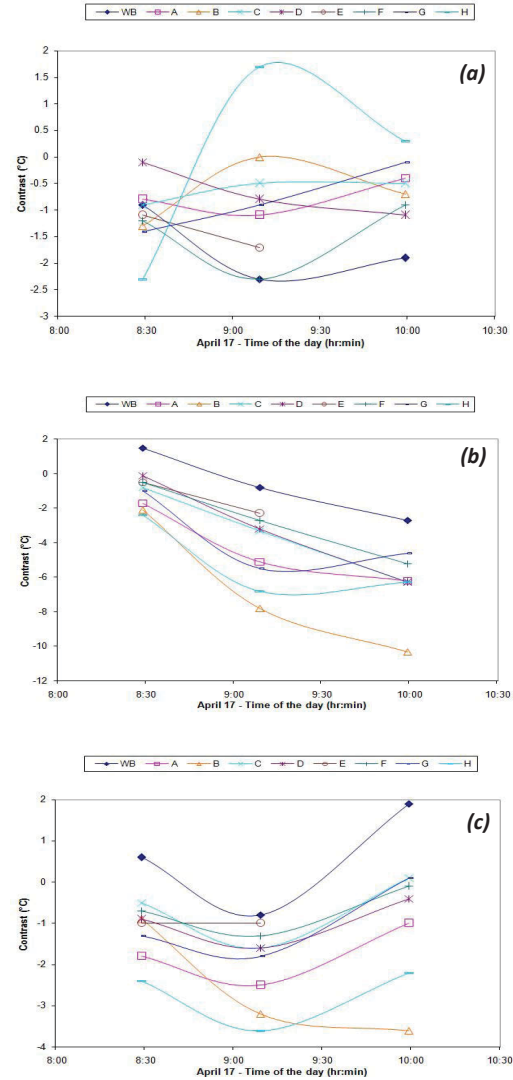


Figure 10. Calculated contrast between disturbed and undisturbed regions of (a) sand; (b) soil; and (c) sand/soil samples with different IR filters.

The trends of the curves are again very similar. In general, the contrast is less compared to those measured the day before around noon time. Most measured contrast values should not be considered as "positive detection" as they lay above or below 0 °C, and are about one or two times of the corresponding NETD associated with the filters used (Tab. 2). However, Filter A and particularly Filter B seemed to bring out the disturbed region contrast in soil and sand/soil samples more than in WB measurement.

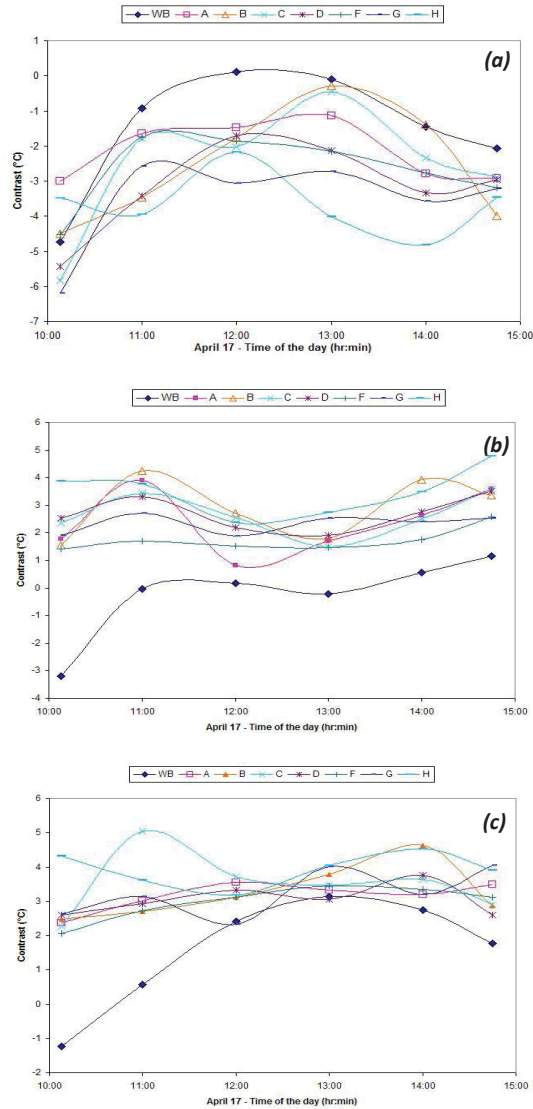


Figure 11. Calculated contrast between disturbed and undisturbed regions of (a) sand; (b) soil; and (c) sand/soil samples with different IR filters.

Fig. 11 (a) to (c) show the contrast characteristics of the three samples on April 17 2008 with different IR filters as a function of time followed by disturbance at around 10h08. In these analyses, more data points were computed using WinSAS to obtain more details. Although transient points were showed with more data points plotted, the trends of the curves are still following those obtained on April 16. In general, all contrast began with the most negative values of the day. It is because all overturned sand, and/soil and soil regions are relatively colder. However, they are less negative and this could be attributed to the warmer ambient temperature.

The sand sample contrast, similar to April 16 measurement, became less negative, or decreased, toward midday as the cold, disturbed regions heated up together with the undisturbed regions. The apparent temperature of the disturbed region barely reach that of the undisturbed region at 12h00 only to drop beyond this point. This showed that the contrast of sand sample was not influenced by the change of ambient temperatures (Fig. 9 (a) and Fig. 11 (a)).

The disturbed sand/soil sample showed largest contrast among the three samples. In the sand/soil sample, all contrast measured with filters began in positive values (disturbed region is hotter than background) except the WB measured value. In addition, we could see that the temperatures of all samples increased during the day and all reached higher temperatures that those measured on April 16, again due to higher ambient temperatures. In some cases, the estimated, absolute temperatures of background and overturned regions (sand, soil) were both higher than those of sand/soil samples. However, the contrast of sand/soil samples is larger than those of sand and sand/soil samples. This could be attributed possibly to the fact that the water presence in the soil and the increased emissivity of the disturbed region (reststrahlen band) resulted in higher contrast.

Filters A, B and C provided significant positive contrast throughout the measurement (Fig. 11 (c)). On the other hand, the contrast of soil sample was always lower than that of sand/soil sample, similar observation from the measurement on April 16.

It is noted that the difference here is less than that measured on April 16 and this could be attributed to the warmer ambient temperatures which brought up the background temperatures and even more the initial temperature of buried-then-overturned soil and sand/soil samples.

4.3. Experimental Data Analysis – Contrast and Wavelength Relationship (Reststrahlen)

We now further examine the spectral contrast curves to see if any contrast difference presents between the use of WB, and IR bandpass filters, particularly Filters A to E covering 8 to 9.5 μm where the reststrahlen band locates.

In Fig. 9 (a), all the curves obtained with filters present less negative contrast than that of the curve obtained in WB. This means that the

disturbed region was apparently hotter than the undisturbed region with filters than in WB. Referring to Fig. 1 on spectral emissivity of disturbed and undisturbed sand, the apparent temperature measured by the IR camera would be colder in the undisturbed region and less cold in the disturbed region when using IR filters in the 8.5 to 9.5 μm with black body reference temperatures. However, since the disturbed region temperature was colder to begin with than that of the undisturbed region, the resulting contrast became less obvious considering possible reststrahlen effect contribution, i.e. the potential enhancement on contrast due to reststrahlen effect could be masked. If the overturned sand portion was at least the same temperature of that of the undisturbed region, the contrast could have increased with the reststrahlen effect contribution, possibly leading to positive contrast. Therefore, the relative temperature between the disturbed and undisturbed regions must be known to interpret the measurement data and reststrahlen effect. The conclusion is that we cannot examine only the contrast.

Since we do not have the spectral emissivity data of the samples, we could not make temperature comparison as a function of wavelengths across the three samples. However, we can still make comparison of spectrally apparent temperature of the same sample (same material composition and same spectral emissivity). By looking at the apparent temperatures, we can examine the reststrahlen effect beginning at 8.6 μm (Filter A). The apparent temperatures of undisturbed and disturbed sand regions measured at wide band and various band pass filters at 11h20, 13h00 and 14h00 were plotted in Fig. 12 (a), (b) and (c).

At 8.6 μm , at 11h20 (Fig. 12 (a)) the apparent temperature of the undisturbed sand region (27.8 $^{\circ}\text{C}$) was lower than that measured at WB (32.2 $^{\circ}\text{C}$) while the disturbed sand region showed as well lower temperature (23.1 $^{\circ}\text{C}$) than that measured at wide band (26.7 $^{\circ}\text{C}$). It is noted, again comparing temperatures between WB and Filter A, that the decrease in temperature is apparently more in undisturbed sand region at 4.4 $^{\circ}\text{C}$ (32.2-27.8 $^{\circ}\text{C}$) measured between WB and Filter A than that in disturbed sand region at 3.6 $^{\circ}\text{C}$ (26.7-23.1 $^{\circ}\text{C}$). This could be attributed to the higher emissivity (reststrahlen effect) of disturbed sand region at this wavelength. This showed that any existing reststrahlen effect in combination of the use of a filter to examine it may in fact reduce the apparent contrast in this case (cold overturned

sample) leading to lower probability of detection, which are -5.5 and -4.7 $^{\circ}\text{C}$ in WB and with Filter A, respectively. If the overturned sand region were warmer to begin with or about the same temperature as the background, the measured contrast in WB might have been around zero or slightly positive while that measured with Filter A might have been positive and larger than that measured in WB. This would have allowed a contrast measurement alone to show any existing reststrahlen effect and positive sand disturbance detection.

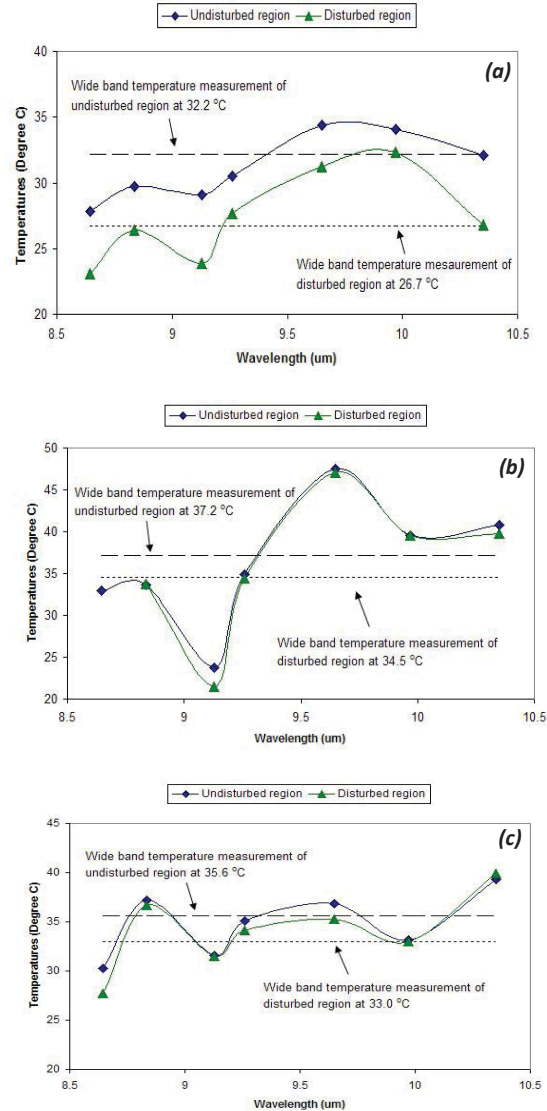


Figure 12. Estimated temperatures in WB and with different IR filters between disturbed and undisturbed regions of sand sample measured at (a) 11h20; (b) 13h00 and (c) 14h00 on April 16.

At both 8.8 and 9.1 μm , the temperature decrease of disturbed sand region ($26.7-26.4=0.3$ and $26.7-23.9=2.8$ $^{\circ}\text{C}$) was still less than that of the undisturbed sand region ($32.2-29.7=2.5$ and $32.2-29.1=3.1$ $^{\circ}\text{C}$). As suggested above, this could be attributed to the higher emissivity (reststrahlen effect) of disturbed sand region at this wavelength.

At both 8.8 and 9.1 μm , at 13h00 (Fig. 12 (b)) the apparent temperature of disturbed and undisturbed sand regions was lower than those measured in WB. The temperature decrease in disturbed sand region ($34.5-33.7=0.8$ $^{\circ}\text{C}$ at 8.8 μm and $34.5-21.5=13.0$ $^{\circ}\text{C}$ at 9.1 μm) was still less than those of the undisturbed sand region ($37.2-33.6=3.6$ $^{\circ}\text{C}$ at 8.8 μm and $37.2-23.7=13.5$ $^{\circ}\text{C}$ at 9.1 μm) meaning the disturbed region was apparently warmer than the undisturbed region possibly due to reststrahlen effect. However, at 9.1 μm , the difference of temperature decrease of disturbed sand region between WB and filtered values is only 0.5 $^{\circ}\text{C}$ ($13.5-13.0$), which is near to the modified NETD value of the filter (665mK, Filter C in Tab. 1). As a result, we could not conclude if reststrahlen effect was observed.

As solar radiation increased and heated up the sand sample, the difference between the WB temperatures of disturbed and undisturbed regions was only at 2.7 $^{\circ}\text{C}$, rather than 5.5 $^{\circ}\text{C}$ at 11h00. This smaller temperature difference led to the fact that the disturbed and undisturbed temperatures, measured using higher center wavelength bandpass filters beyond the reststrahlen region, converged and merged together, i.e. the apparent temperatures were the same at longer wavelengths. The measured temperatures of both disturbed and undisturbed regions still approached close to the temperatures measured at WB. The overshoot above the wide band measured temperatures at 9.6 μm was observed here as well.

The apparent temperatures of undisturbed and disturbed sand regions measured at WB and various band pass filters at 14h00 were shown in Fig. 12 (c). Based on the analysis, we did not see possible reststrahlen effect at 8.6 μm . At 8.8 μm , the apparent temperature of disturbed and undisturbed regions was higher than that measured at WB. As described above, a clearer sign of increased contrast for sand disturbance detection was shown this time as the disturbed region apparent temperature was 3.7 $^{\circ}\text{C}$ higher at 8.8 μm than that measured at WB while the undisturbed region was 1.6 $^{\circ}\text{C}$ higher. This could

be attributed to the reststrahlen band. At 9.1 μm , the apparent temperature of disturbed and undisturbed regions was again lower than that measured at WB. This time, the disturbed region apparent temperature was 1.5 $^{\circ}\text{C}$ lower at 9.1 μm than that measured at WB while the undisturbed region was 4.0 $^{\circ}\text{C}$ lower. This means that the disturbed region at 9.1 μm , the reststrahlen band, was again warmer. At longer wavelengths, the disturbed and undisturbed temperatures measured using higher center wavelength band pass filters converged and merged together as previously observed.

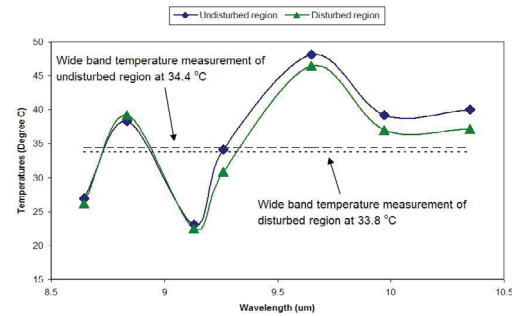


Figure 13. Estimated temperatures in WB and with different IR filters between disturbed and undisturbed regions of soil sample measured at 13h00 on April 16.

In the following morning on April 17 (8h30, 9h10, 10h00), based on the same analysis, it is inconclusive if reststrahlen effect is present in the sand sample with respect to the apparent temperatures and camera sensitivity with the use of IR bandpass filters. For the soil sample, it seems that possible reststrahlen effect was only observed on April 16 at 13h00 using the 8.8 μm bandpass filter (Fig. 13) as the disturbed soil region was 5.4 $^{\circ}\text{C}$ warmer than that measured at WB compared to 3.9 $^{\circ}\text{C}$ in the case of undisturbed soil region. Beyond this point, the apparent temperatures of both undisturbed and disturbed soil regions followed similar pattern including the overshooting and closing in to those measured at WB at longer wavelengths. Other results are inconclusive. For the sand/soil sample, the disturbed region was clearly warmer than the undisturbed region seen at WB on April 16 at 13h00 and 14h00 (Fig. 14 (a) and (b)). This could be due to the fact that the water in the sample absorbed enough solar radiation to reach elevated temperatures. In the case of soil sample, the larger water content (high heat capacity) required more absorbed energy to reach higher temperatures. The disturbed region temperature did approach to that of undisturbed region in WB, only to decrease again (e.g. Fig. 13).

Here, the disturbed region temperatures did reach higher than those of undisturbed region, i.e. a positive contrast. As previously mentioned, this allows the observation of contrast only for possible ground disturbance detection. In fact, if we examined the temperature decrease (or increase in several wavelengths at 13h00) of disturbed and undisturbed regions from the associated WB to filtered measurement, the disturbed region showed relatively less hot or decrease more, which is contrary to previous discussed cases.

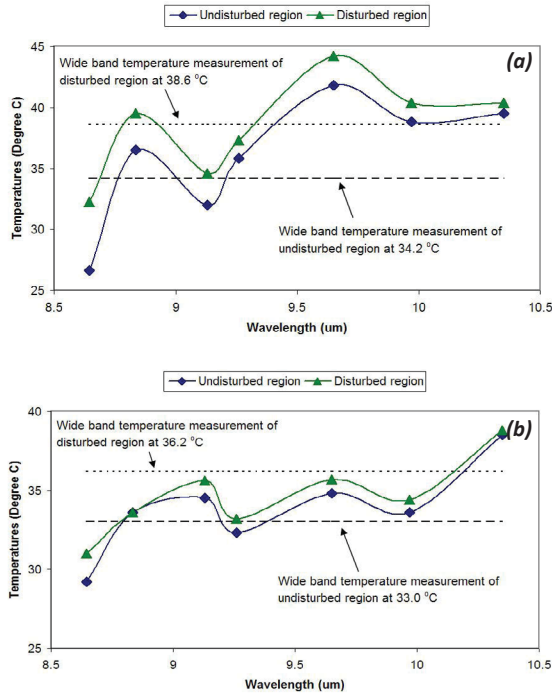


Figure 14. Estimated temperatures in WB and with different IR filters between disturbed and undisturbed regions of sand/soil sample measured at (a) 13h00 and (b) 14h00 on April 16.

This implies that we may first look at contrast and then examine temperature decrease of disturbed and undisturbed regions from associated WB to filtered measurements. Beyond 9.1 μm at longer wavelength, the apparent temperatures of both disturbed and undisturbed regions were again about the same.

4.4. Experimental Data Analysis – Disturbed Region Boundary Detection

In the above sessions, both contrast and apparent temperatures of disturbed and undisturbed samples measured in both WB and with bandpass IR filters were examined. We have seen deviance with the presence of disturbed region in several

conditions possibly due to reststrahlen effect, water content in the samples, or other phenomena. However, due to the complexity of the problem and the interdependence of parameters such as sample type, sample surface and below-the-surface temperature, ambient temperature, etc., we did not see neither clear deviance nor trend in some conditions. For example, as described in Session 4.3, cold, overturned sample may lead to reduced contrast leading to lower probability of ground disturbance detection.

Here, we examined and analyzed the data in a different approach. First, we indicated the regions of the two black bodies and then entered the corresponding temperatures in WinISAS. This time, we marked two small squares horizontally side-by-side for temperature and contrast calculation. We then moved the two squares horizontally to the right by two-square size for another temperature-contrast calculation.

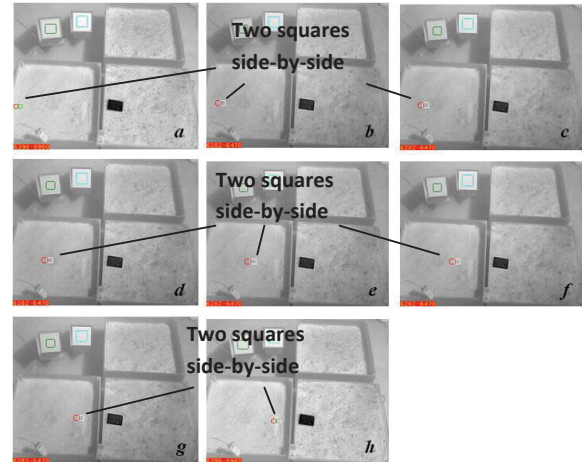


Figure 15. Series of IR images taken in WB mode on April 15 showing the positions of two squares marked for temperature analysis moving across the sand sample from a to h.

We repeated this exercise until we went through the disturbed region. In theory, the contrast is zero when the two squares are located entirely either in the undisturbed or disturbed regions. When the two squares begin entering and leaving the disturbed region, we should see a deviance or contrast. The signs of contrasts should reverse from positive to negative, or vice versa between entry and exit, independent to initial overturned sample temperatures. This exercise may allow a more "straight forward" pattern to possibly detect ground disturbance by examining the change or contrast at the undisturbed-disturbed boundary. This approach may also be more realistic in the field for scan-and-search for disturbed ground.

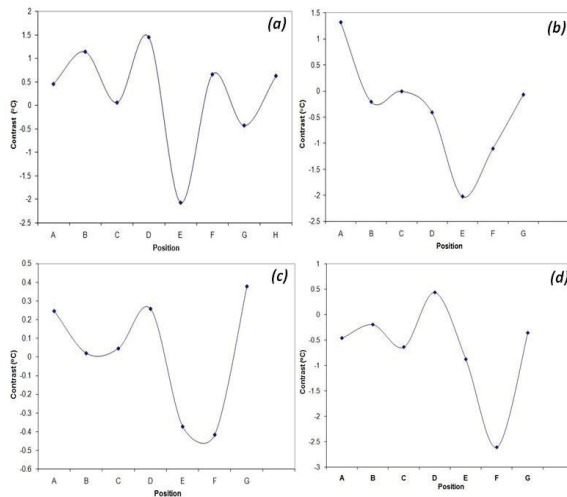


Figure 16. Contrast of the two squares moving through the disturbed sand region at 13h50 April 15 (a) in WB and (b) with Filter E; and at 10h00 April 16 (a) in WB and (b) with Filter E.

Fig. 15 illustrates a series of images, taken around 13h50 on April 15 2008 in WB mode, showing the locations of the two squares moving from Positions a to h across the sand sample. In this case, the center of the sample was disturbed at 13h32 on April 15. Precaution was made so that the disturbed region is indistinguishable in visible before and after the disturbance. Fig. 16 (a) to (d) showed the temperature contrasts of the two squares moving through the disturbed region (center) across the sand sample at 13h50 on April 15 and the day after disturbance at 10h00 on April 16 2008. We analyzed these images following the same scheme above. We could see substantial contrast with WB and Filter E. We also did the same experiments on soil and sand/soil samples but the results were mixed due to the fact that these samples contain small rocks on the surface which leads to frequent contrast fluctuation over the entire scanning. It may be possible to minimize this fluctuation by first performing a background scan before the disturbance to determine a reference.

5. CONCLUSIONS

WB and multispectral imaging showed ground disturbance detection, including reststrahlen effect, in some conditions. However, a good knowledge of the area of operation such as weather condition, temperatures of above and below surface, are required to possibly allow a more robust and reliable measurement. A two-point scanning scheme showed potential advantage on ground disturbance detection.

6. REFERENCES

- [1] Dumas, J. (1996). *Mesure de signatures infrarouges de mines terrestres et expériences de perception*. DREV-R-9525. Defence R&D Canada. 43 pages.
- [2] Simard, J.-R. (1997). *Theoretical and experimental characterizations of the IR technology for the detection of low-metal and nonmetallic buried landmines*. DREV-R-9615. Defence R&D Canada. 104 pages.
- [3] Simard, J.-R. (1997). *Theoretical and experimental characterizations of the IR technology for the detection of low-metal and nonmetallic buried landmines*. DREV-R-9615. Defence R&D Canada. 104 pages ; Russell, K., McFee, J., and Sirovyak, W. (2000). *Remote performance prediction for infrared imaging of buried mines*. DRES-SL-2000-0151. Defence R&D Canada. 10 pages.
- [4] Simard, J.-R. (1994). *Experimental evaluation of the apparent temperature contrast created by buried mines as seen by an IR imager*. DRES-SR-607. Defence R&D Canada. 32 pages.
- [5] Sherbondy, K. (2007). EO-IR diurnal data collections. Presented to The Technical Cooperation Program (TTCP) SEN AG-08 Exploratory group on mine detection. Fort Halstead, United Kingdom 28 February – 1 March 2007.
- [6] (2006). Detection and remediation technologies for mines and minelike targets XI. *SPIE* 6217 ; (2007). Detection and remediation technologies for mines and minelike targets XII. *SPIE* 6553
- [7] McFee, J., Anger, C., Achal, S., and Ivanco, T. (2006). Landmine detection using passive hyperspectral imaging. Presented to *SPIE Defense and Security. Orlando, United State 17-21 April 2006*.
- [8] Cathcart, M. (2007). *Characterization of terrain clutter features in hyperspectral data to aid landmine detection*. Presented to The Technical Cooperation Program (TTCP) SEN AG-08 Exploratory group on mine detection. Fort Halstead, United Kingdom 28 February – 1 March 2007.
- [9] Deas, R. (2007). UK countermine research programme – update. Presented to *The Technical Cooperation Program (TTCP) SEN AG-08 Exploratory group on mine detection*. Fort Halstead, United Kingdom 28 February – 1 March 2007.
- [10] Kelch, D.J., Fatora, D.A., Hill, R.K., Krause, K., Lind, P.R., Siler, E., Sink, B.L., and Sira, D. (1999). The Physical Bases for Exploitable Soil Spectral Signatures. (1999b). *International Society for Strategic Studies in Radiology (ISSR) 1999. Las Vegas, United State, 31 October – 4 November 1999*.
- [11] Milton, A. (2004). US Army infrared imaging (and QWIP). *International Workshop on Quantum Well Infrared Photodetectors QWIP2004*. Alberta, Canada 8-13 August 2004.
- [12] Winter, E.M., Lucey, P.G., and Winter, M.E. (2001). The analysis of data from a thermal infrared hyperspectral instrument. *SPIE* 4151, 256-264.
- [13] <http://www.icess.ucsb.edu/modis/EMIS/html/soil.html>